View Article Online
View Journal

Chemical Science

Accepted Manuscript

This article can be cited before page numbers have been issued, to do this please use: Y. Yin, H. Zhao, Z. Yu, G. Ge, H. Zhou, K. Sun, S. Feng, J. Du, T. Chen, Z. Yang, J. Yu and S. Mu, *Chem. Sci.*, 2026, DOI: 10.1039/D5SC06809F.

View Article Online
DOI: 10.1039/D5SC06809F

Received 00th January 20xx,
Accepted 00th January 20xx

DOI: 10.1039/x0xx00000x

Electron-enrichment Enables RuPd toward 1.406 V Overall Water Splitting

Yuqin Yin[a,b], Hongyu Zhao[a,b], Zhanghu Yu[a,b], Guanren Ge[a,b], Shiyuan Feng[c], Haoyu Zhou[c], Kaiyang Sun[d], Jie Du[a,b], Tong Chen[a,b], Zhihao Yang[a,b], Jun Yu[a,b]*, Shichun Mu[a,b]*

The development of cost-effective and stable bifunctional catalysts is crucial for reducing the cost of green hydrogen production via water electrolysis. Herein, we report a RuPd-RuNiFeO$_x$ catalyst supported on nickel foam, synthesized via a facile non-homogeneous nucleation method. The catalyst exhibits exceptional hydrogen evolution (HER, 17 mV@10 mA cm^{-2}) and oxygen evolution (OER, 263 mV@50 mA cm^{-2}) activities in alkaline freshwater, requiring only 1.406 V for overall water splitting at 10 mA cm^{-2} with outstanding stability over 100 h. Remarkable performance is also demonstrated in seawater electrolysis. Combined experimental characterization and density functional theory (DFT) calculations reveal that the superior activity and stability originate from electron enrichment at the interfacial Ru sites, driven by charge redistribution from the NiFeO$_x$ support to the RuPd cluster. This electron enrichment optimizes the d-band center of Ru, yielding a near-ideal hydrogen adsorption free energy ($\Delta G_{H*} \approx -0.10$ eV) and significantly reduces energy barriers for both water dissociation and the OER rate-determining step. This work provides a mechanistic understanding and a practical strategy for designing high-performance, durable catalysts for sustainable hydrogen production.

1. Introduction

Low-temperature water electrolysis allows for the rapid production of green hydrogen as an ideal method for storing renewable energy sources such as wind and solar in future clean energy infrastructures.[1–3] Electrochemical water splitting typically consists of two half-reactions: oxygen evolution reaction (OER) and hydrogen evolution reaction (HER). Efficient overall water splitting requires the use of bifunctional electrocatalysts with high HER and OER activities to reduce the reaction barrier.[4–6] In addition, although seawater, as an abundant natural resource accounting for 96.5% of the total global water resources, large-scale seawater water electrolysis still faces significant challenges due to its complex composition.[7–11] To date, iridium (Ir)- and platinum (Pt)-based materials are the best catalysts for OER and HER, respectively. However, their high cost and limited reserves have seriously hindered the widespread application of water electrolysis technology.[12] In addition, most catalysts can only exhibit the single performance of HER or OER in the same medium, which undoubtedly increases the difficulty of industrial hydrogen production. Therefore, the development of cost-effective bifunctional catalysts is imminent.

Ruthenium (Ru), which is only 1/4 of the price of Pt, has aroused widespread interest.[13] However, although Ru-based catalysts possess high catalytic activity, the low electrochemical stability restricts their application in practical electrochemical reactions. To break through the performance limitation of Ru-based catalysts, Ru-based composite catalyst systems have been developed. Among them, alloying Ru with other Pt-group metals (e.g., Pt, Ir, etc.) or constructing heterostructures is a promising strategy.[14,15] However, the oxidation of Ru at high potentials (from tetravalent to octavalent) and the subsequent precipitation of dissolved Ru can lead to the deactivation of Ru-based catalysts.[16] Therefore, the design of suitable support materials that can effectively stabilize Ru species is essential for optimizing dispersion problems, reducing particle size, and increasing the density of active sites and cycling durability.

Among various support materials, three-dimensional transition metal oxides containing different metals (e.g., cobalt, nickel, iron, etc.) are promising for electrocatalysts due to their unique layered structures and abundant active sites, wherein nickel (Ni)-iron (Fe) oxides are regarded as ideal catalyst carriers due to their highly efficient OER activity and stability.[17] However, their intrinsic HER activity is severely insufficient, which limits their applications in water electrolysis.[18] To overcome these limitations, various strategies have been proposed to enhance the catalytic performance

---

[a] *State Key Laboratory of Advanced Technology for Materials Synthesis and Processing, Wuhan University of Technology, Wuhan 430070, China.*
[b] *Key Laboratory of Fuel Cell Technology of Hubei Province, Wuhan 430070, China.*
[c] *School of Materials Science and Engineering, Wuhan University of Technology, Wuhan 430070, China.*
[d] *College of Chemistry & Chemical Engineering, Northwest Normal University, Lanzhou 730000, China.*
[e] *Y Yin and H Y Zhao contributed equally to this work.*
*E-mail: msc@whut.edu.cn , yujun@whut.edu.cn

Supplementary Information available: [details of any supplementary information available should be included here]. See DOI: 10.1039/x0xx00000x

View Article Online
DOI: 10.1039/D5SC06809F

of nickel-iron oxides. For example, by filling the oxygen vacancy in them with atoms such as Ru, phosphorus (P), and sulfur (S), both the activity and stability of Ni-Fe oxides have been enhanced.[19–21] In addition, it was shown that Ni-Fe mixed oxides with surface oxygen vacancies prepared by a simple two-step thermal-assisted method exhibited excellent electrocatalytic properties. This method not only optimized the precursor composition and calcination temperature but also improved the electrocatalytic performance through nanosizing and porous structure formation.[22] It was also found that the activity of Fe-doped β-nickel oxyhydroxides strongly depends on the crystallographic facets. Doping on certain crystallographic facets can significantly reduce the thermodynamic overpotential and thus increase the HER activity.[23] Thus, the catalytic property of Ni-Fe oxides can be improved by elemental doping, precursor optimization and other strategies, which provide new possibilities for applications in water electrolysis.

Herein, we aim to achieve electron enrichment at the Ru active sites-a targeted electronic state where Ru gains increased electron density through interfacial charge transfer from a tailored support-to simultaneously modulate adsorption energetics and enhance electrochemical stability.

To this end, this work innovatively introduces Ru and palladium (Pd) on to the NiFe oxide substrate through the strategy of strain and electron synergistic modulation in polymetallic oxides to achieve electron enrichment at the RuPd site and construct a RuPd-RuNiFeO$_x$/NF catalyst where Ru is dispersed in Pd clusters and amorphous NiFeO$_x$.[24] The design is based on three considerations: First, to enhance HER activity under alkaline conditions, Ru, as a larger element, is selectively introduced to the NiFeO$_x$/NF surface to generate strain, oxygen vacancies (O$_{Vs}$), and active sites.[25] Second, to enhance desorption kinetics and Ru stability under alkaline conditions, Pd with a mixed-valence oxidation state of Pd $^{\delta+}$ is also introduced to the NiFeO$_x$ surface.[26] This facilitates the adsorption of oxygen-containing intermediates in the OER process and the dissociation of H_2O in HER, and inhibits the overoxidation of Ru due to its high electronegativity. Third, the charge redistribution at the RuPd/RuNiFeO$_x$ interface synergistically accelerates the reaction path and increases the oxygen vacancy concentration in the process, this is conducive to electronic distribution and interfacial charge transfer during the catalysis process simultaneously enhancing the performance of water/seawater electrolysis.[27]

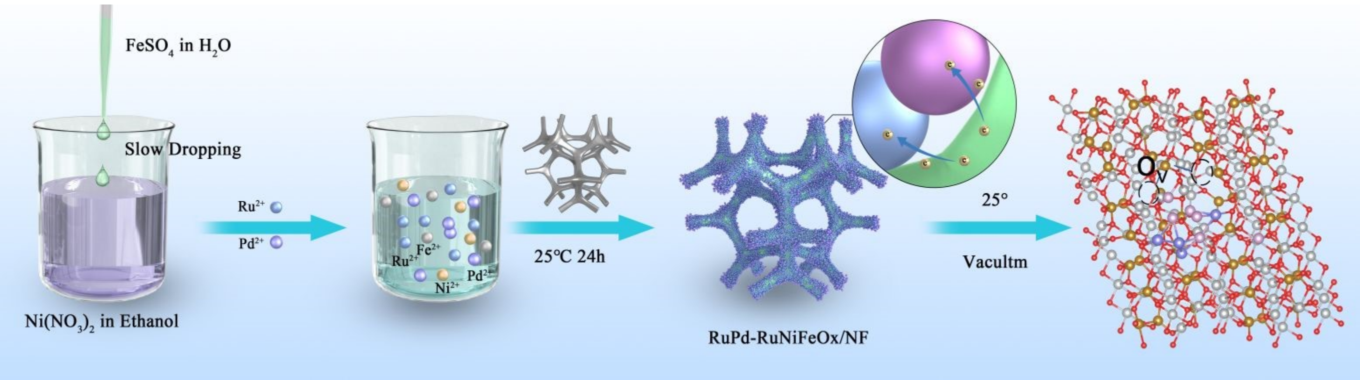

Scheme 1. Synthetic illustration of RuPd-RuNiFeO$_x$/NF catalyst.

2. Results and Discussion

2.1 Catalysts Synthesis and characterization.

The synthesis process of the catalyst is shown in **Scheme 1**. By a non-homogeneous nucleation method, an aqueous solution of FeSO$_4$ was slowly added to an ethanol solution of Ni(NO$_3$)$_2$, which resulted in the formation of insoluble nanoparticles due to the poor solubility of sulfate in organic solvents.[28] The nanoparticle adsorbed on the surface of the NF, which reduced the interfacial energy and acted as nuclei without the need for a basic nucleation process. Subsequently, RuCl$_3$-xH$_2$O and PdCl$_2$-xH$_2$O were introduced into the above solution, and the nickel foam (NF) was immersed in the liquids for 24 h at 25°C., the non-homogeneous nucleation method was used to easily prepare large-sized catalysts with uniform distribution on nickel substrates (Figure S1, Supporting Information). Scanning transmission electron microscopy (STEM) images show that these insoluble nanoparticles were widely and uniformly distributed, with an average diameter of 3.84 ± 0.02 nm (Figure S2, Supporting Information) The solution was measured by inductively coupled plasma mass spectrometry (ICP-OES) to have a Ni/Fe atomic ratio is 5.74 (Figure S3, Supporting Information). The whole synthesis process was completed at room temperature and atmospheric pressure without harsh operation. In addition, to investigate the effect of Ru/Pd doping, Ru-NiFeO$_x$/NF, Pd-NiFeO$_x$/NF and NiFeO$_x$/NF were synthesized in the absence of RuCl$_3$-xH$_2$O and PdCl$_2$-xH$_2$O, respectively. For comparison, RuPdO$_x$ was synthesized without addition of Ni(NO$_3$)$_2$ and FeSO$_4$.

X-ray diffraction (XRD) patterns confirm that there is only one set of interfacial angles located at 44.5°, 51.8°, and 76.4° (Figure S4, Supporting Information), which corresponds to the (111), (200), and (220). Such diffraction peaks can be indexed to the metallic Ni originated from the nickel foam substrate (JCPDS No. 87-0712), suggesting the amorphous nature of RuPd-RuNiFeO$_x$. To determine the microscopic morphology of RuPd-RuNiFeO$_x$/NF, field emission scanning electron microscopy (FE-SEM), TEM, and spherical aberration-corrected atomic resolution HAADF-STEM were used for structure characterization. SEM images of NiFeO$_x$/NF (Figure S5, Supporting Information) and RuPd-RuNiFeO$_x$/NF (**Figure 1a**, Figure S6, Supporting Information) show that after the Ru and Pd doping, the nanosheet of the sample is altered greatly, and the morphology of the catalyst changes from a continuous, interwoven nanofiber

View Article Online
DOI: 10.1039/D5SC06809F

network to a nanoflower-like nanoparticle agglomerate. The TEM image (**Figure 1b**) further confirms the nanoflower structure of RuPd-RuNiFeO_x. The elemental mapping of RuPd-RuNiFeO_x determined by the TEM image (**Figure 1c**) reveal the uniform distribution of elemental Pd, Ru, Ni, and Fe on the nanoflower. The selected area electron diffraction (SAED) pattern of RuPd-RuNiFeO_x/NF (**Figure 1d**) indicates its amorphous nature, consistent with the previous XRD analysis results. From HAADF-STEM images, there are distinct cluster and amorphous regions in **Figure 1e**. For the cluster, its lattice spacing of 0.221 nm corresponding to the (111) crystalline plane of Pd in RuPd-RuNiFeO_x/NF, which is wider than that of the lattice spacing of the standard Pd (0.22 nm), suggesting that the doping of Ru generates typical lattice strain in Pd clusters. [29]For the amorphous region, it could be attributed to NiFeO_x as support of RuPd clusters. From the HAADF-STEM image with spherical aberration correction (**Figure 1f**), isolated metal (Ru or Pd) single atoms are uniformly distributed as bright spots on the surface of RuPd-RuNiFeO_x/NF. Furthermore, RuPd-RuNiFeOx identified through HAADF-STEM images (**Figure 1g**) and corresponding elemental mapping (**Figure 1h**) reveal that the elements of Ni and Fe are uniformly distributed on the nanoflower, whereas Ru is uniformly dispersed on Pd clusters and substrate in the form of monoatoms. The Ru and Pd content of RuPd-RuNiFeO_x/NF was determined to be 3.4 and 4.1 wt%, respectively, by ICP-OES analysis (Figure S7, Supporting Information).

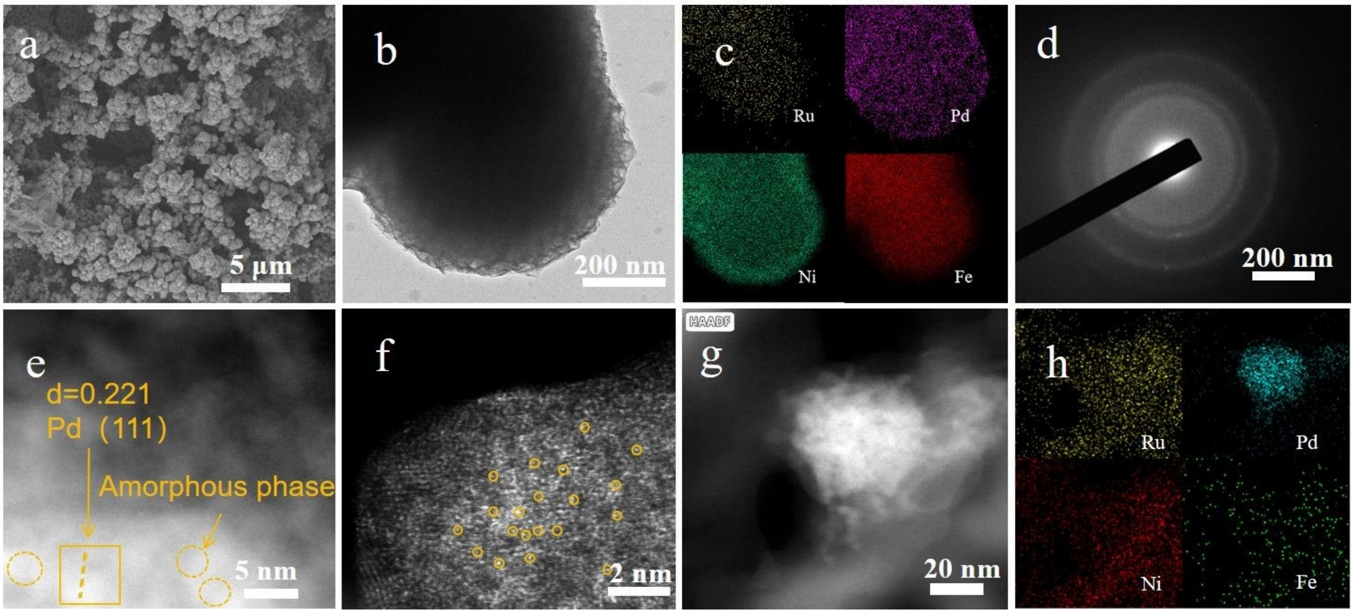

Fig. 1 a) SEM image of RuPd-RuNiFeOx/NF. b) TEM image of RuPd-RuNiFeO_x. c,h) EDS mapping of RuPd-RuNiFeOx. d) Selected-area electron diffraction (SAED) pattern of RuPd-RuNiFeO_x. e,f,g) Spherical aberration-corrected atomic resolution HAADF-STEM image of RuPd-RuNiFeOx/NF.

As seen in X-ray photoelectron spectroscopy (XPS), RuPd-RuNiFeO_x/NF consists of elemental Ru, Pd, Ni, Fe, and O (Figure S8, Supporting Information), whereas NiFeO_x does not contain elemental Ru and Pd, which indicates the successful introduction of Ru and Pd on NiFeO_x. The XPS elemental semi-quantitative results show only 0.29 at% of Ru and 1.45 at% of Pd (Table S1), which again indicates that the precious metal content in this catalyst is extremely low. In the spectra of Ni elements (**Figure 2a**), the peaks located at 855.78 and 873.35 eV correspond to Ni^{2+} $2p_{3/2}$ and Ni^{2+} $2p_{1/2}$, respectively, and the two peaks at 861.4 and 878.2 eV are satellite peaks of Ni 2p. In **Figure 2b**, the peaks at 711.56 and 724.36 eV correspond to $Fe^{3+}2p_{3/2}$, and the peaks at 707.09 and 719.89 eV are attributed to Fe^{2+}. In addition, the Ru3p mapping (**Figure 2c**) shows the presence of characteristic peaks in the Ru3p orbitals at 462.3 ($3p_{3/2}$) and 485.8 eV ($3p_{1/2}$), which correspond to the metallic state Ru^{4+}.[30] The weaker peak intensity stems from the low loading of Ru, which was confirmed to be dispersed in monoatomic form in combination with HAADF-STEM (**Figure 1h**). **Figure 2d** shows the presence of characteristic double peaks in the Pd 3d orbitals at 335.03 ($3d_5/_2$) and 340.48 eV ($3d_3/_2$), which correspond to the metallic state Pd^0, respectively. [31] The binding energy is positively shifted by 0.07 eV compared to bulk Pd (335.1 eV), which is attributed to the nanoscale effect and the electronic interaction between Pd and substrate (NiFeO_x). The O1s XPS spectra (**Figure 2e**) exhibit three characteristic peaks: the M-O bond (530.0 eV), the oxygen vacancy (531.5 eV), and the O-H (533.0 eV). Compared with sample NiFeO_x/NF, for the O1s XPS of RuPd-RuNiFeO_x, the overall negative shift of the oxygen spectral band is 0.5 eV, and the intensity of the oxygen vacancy peak increases., indicating that the formation of oxygen vacancies and the electron redistribution alter the chemical environment of the support. This electron reorganization facilitates the electron transfer from the support to the RuPd sites. This is further supported by the electron paramagnetic resonance (EPR) (**Figure. 2f**) results where the EPR peak intensity of RuPd-RuNiFeO_x/NF is significantly higher than that of the other samples, suggesting that the introduction of Ru and Pd does produce more oxygen vacancies (O_{Vs}). This phenomenon is self-corroborating with the positive shift (electron loss) of Ni 2p/Fe 2p and the negative shift (electron gain) of Ru/Pd. This directional flow of electrons increases the interaction between RuPd sites and NiFeO_x and the intrinsic activity of the catalyst, resulting in a lower water splitting energy barrier.

View Article Online
DOI: 10.1039/D5SC06809F

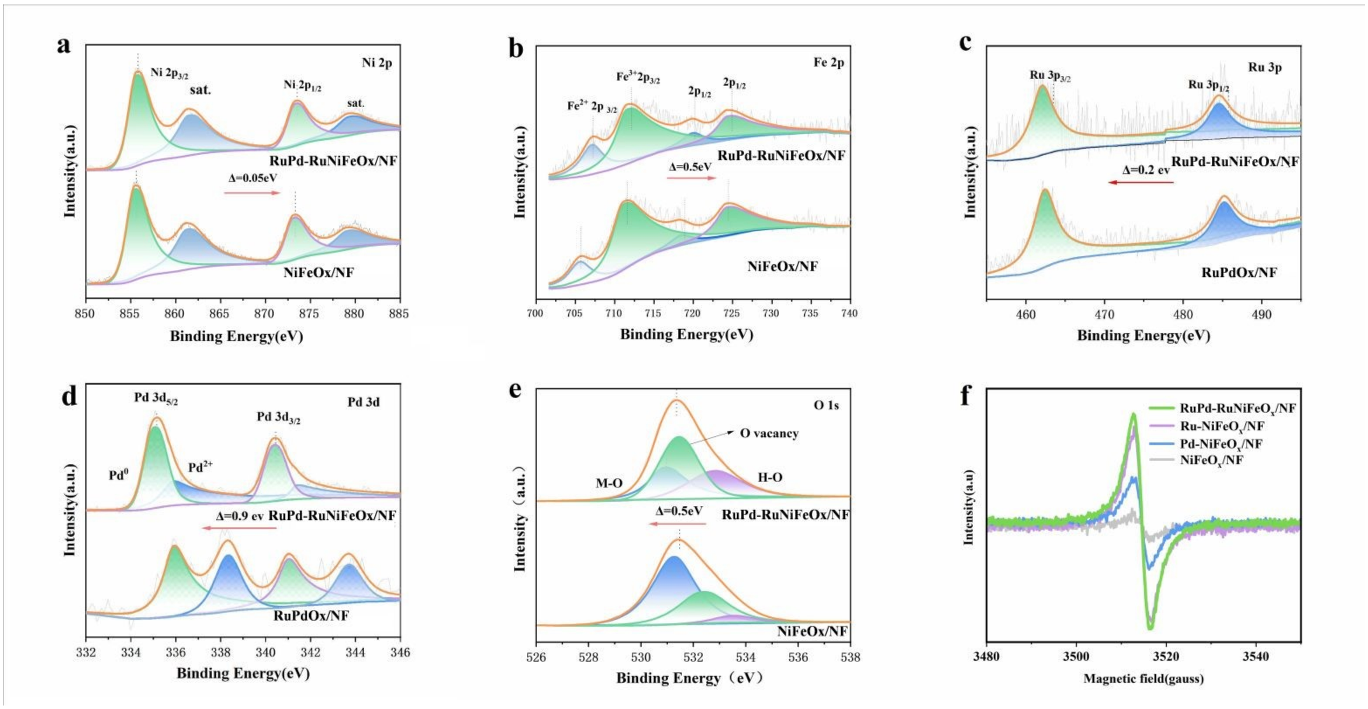

Fig. 2. (a-e) High-resolution XPS comparison spectra of RuPd-RuNiFeO$_x$/NF, NiFeO$_x$/NF and RuPd/NF. (a) Ni2p, (b) Fe2p, (c) Ru3p, (d) Pd3d, (e) O1s, (f) EPR.

2.2 Electrocatalytic properties of hydrogen evolution and oxygen evolution reactions.

The HER behavior of catalysts was first investigated in a standard three-electrode system and 1 M KOH freshwater. As shown in **Figure 3a**, the HER activity is as follows: RuPd-RuNiFeO$_x$/NF> Pt/C on NF> Ru-NiFeO$_x$/NF > Pd-NiFeO$_x$/NF > NiFeO$_x$/NF. Among them, RuPd-RuNiFeO$_x$/NF shows the highest catalytic activity, which requires only 17 and 55 mV overpotentials to achieve current densities of 10 and 50 mA cm^{-2} (**Figure 3b**), respectively, much lower than that of commercial Pt/C (27 and 71 mV), Ru-NiFeO$_x$/NF (40 and 89 mV), Pd-NiFeO$_x$/NF (65 and 131 mV), and NiFeO$_x$/NF (103 and 162mV). At larger current densities, RuPd-NiFeO$_x$/NF still outperforms the control samples. The excellent HER performance is also superior to the recently reported noble metal catalysts (Table S2, Supporting Information). As shown in **Figure 3c,** the Tafel slope of RuPd-RuNiFeO$_x$/NF is the smallest, which indicates an optimal electrocatalytic kinetics compared to the control sample. Meanwhile, RuPd-RuNiFeO$_x$/NF exhibits the smallest charge transfer resistance (R$_{ct}$), suggesting an extremely high charge transfer capability (**Figure 3d**). In addition, the bilayer capacitance was calculated by cyclic voltammetry (CV) curves at successive scanning speeds in the non-Faraday region (Figure S9, Supporting Information). As present in **Figure 3e**, the C$_{dl}$ value of RuPd-RuNiFeO$_x$/NF (235.5 mF cm^{-2}) is much higher than that of Ru-NiFeO$_x$/NF (33.6 mF cm^{-2}), Pd-NiFeO$_x$/NF (17.95 mF cm^{-2}) and NiFeO$_x$/NF (17.73 mF cm^{-2}). Subsequently, C$_{dl}$ was utilized to reflect the electrochemically active surface area (ECSA), which indicates that RuPd-RuNiFeOx/NF has the highest intrinsic activity (Table S3, Supporting Information).

As shown in **Figure 3f**, the linear scanning voltammetric (LSV) curve of RuPd-RuNiFeO$_x$/NF before and after 5000 cycles shows only a slight shift. In addition, the chronoamperometric test (**Figure 3g**) presents that the catalyst can maintain a stable catalytic performance up to 100 h. This confirms the excellent long-term stability of RuPd-RuNiFeO$_x$/NF. After HER test, it can be observed that RuPd-RuNiFeO$_x$/NF still owns a pristine nanoparticle agglomerate after the 100 h HER test (Figure S10, Supporting Information). Figure S11 shows the XPS spectra of the elemental Ni, Fe, Ru, and Pd. As expected, there is no significant change in the Ni2p spectrum, indicating that the surface Ni composition was not changed. In contrast, the peak of Fe2p decreased significantly, marking that the precipitation of Fe occurred during the hydrogen evolution process. Meanwhile, the negative peak shift of Ru3p and Pd3d peaks can be attributed to the reduction reaction during HER, which indicates that Ru and Pd are the active species for electrochemical hydrogen evolution. [32] This further proves that NiFeO$_x$ as support provides electrons to Ru and Pd evidenced by a negative shift of binding energy for Ni2p and Fe2p peaks), which enhances the hydrogen evolution activity of Ru and Pd sites. The single-metal catalyst (Ru/Pd-NiFeO$_x$) is limited in activity due to the incomplete reaction path, while NiFeO$_x$/NF lacks metal sites, resulting in the lowest activity. In addition, the Raman spectra before and after HER do not show significant changes, further demonstrating the excellent stability of the catalyst (Figure S12, Supporting Information).

View Article Online
DOI: 10.1039/D5SC06809F

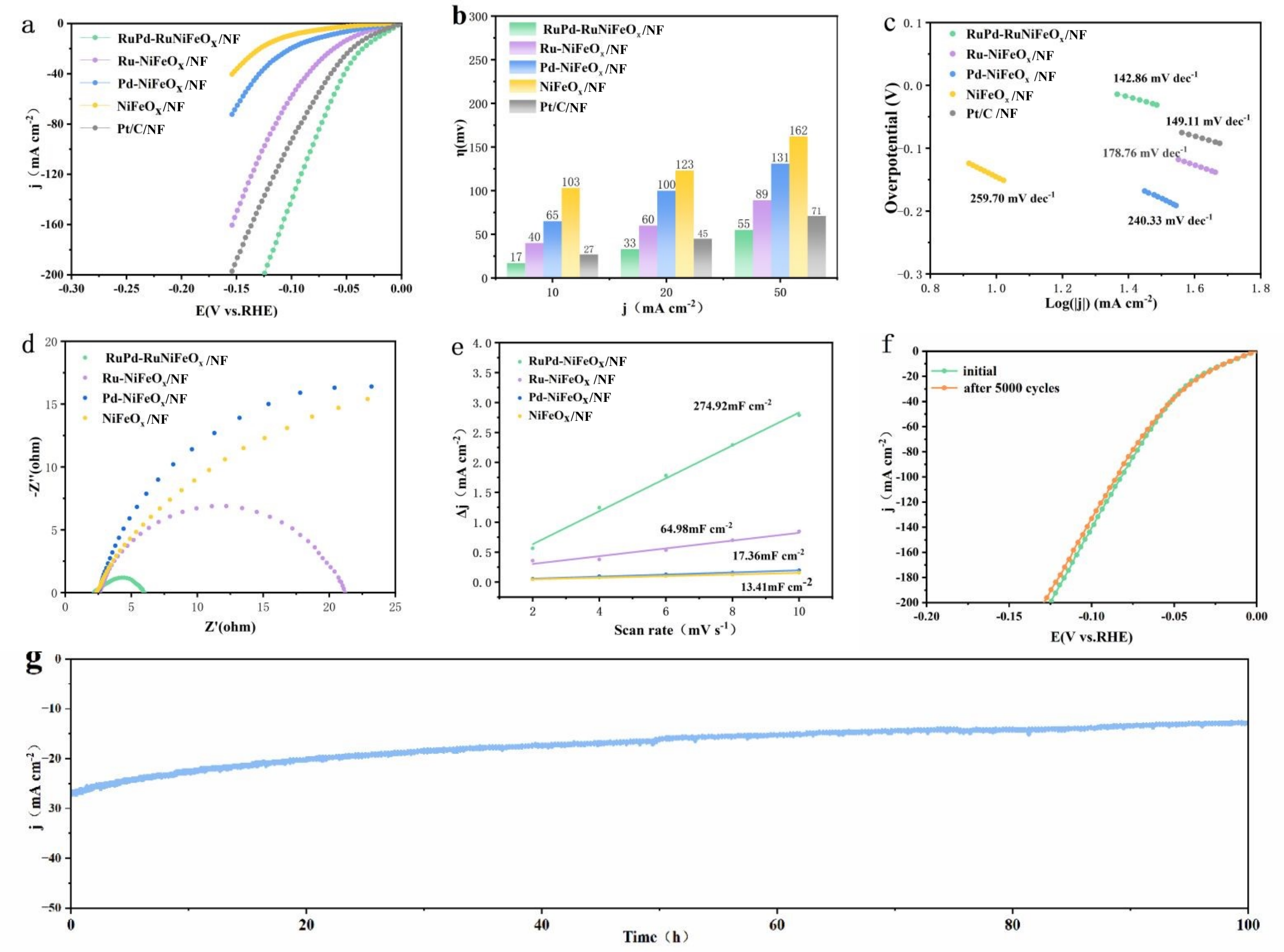

Fig. 3 a) HER polarization curves of various catalysts in alkaline freshwater. b) Tafel slope. c) Corresponding overpotentials. d) Nyquist plots. e) Plots of current density versus scan rate for various catalysts. f) LSV curves initially and after cycles of cyclic voltammetry. g) I-t tests of RuPd-RuNiFeO$_x$/NF.

Similarly, the OER behavior was examined. As shown in Figure **4a**,**b**, the OER performance is ranked as RuPd-RuNiFeO$_x$/NF > Ru-NiFeO$_x$/NF > RuO$_2$ on NF> Pd-NiFeO$_x$ /NF> NiFeO$_x$ /NF. Among them, RuPd-RuNiFeO$_x$/NF exhibits the highest catalytic activity. It requires only 263 and 290 overpotentials to achieve current densities of 50 and 100 mAcm^{-2}, respectively, which is significantly lower than that of commercial RuO$_2$ (279 and 310 mV), Ru-NiFeO$_x$/NF (277 and 308 mV), Pd-NiFeO$_x$/NF (290 and 318 mV), and NiFeO$_x$/NF (280 and 311 mV). At larger current densities, RuPd-NiFeO$_x$/NF still outperforms other catalysts. Such excellent activity is also quite competitive among the recently reported catalysts (Table S4, Supporting Information). As shown in **Figure 4c**, it has the smallest Tafel slope, which indicates a faster electrocatalytic kinetics compared to the control sample. As expected, RuPd-RuNiFeO$_x$/NF exhibits the smallest charge transfer resistance (R$_{ct}$), suggesting a higher charge transfer capability (**Figure 4d**). In addition, according to CV curves (Figure S13, Supporting Information), the C$_{dl}$ value of RuPd-RuNiFeO$_x$/NF (274.92 mF cm^{-2}) was calculated (**Figure 4e**), which is much higher than that of Ru-NiFeO$_x$/NF (64.95 mF cm^{-2}), Pd-NiFeO$_x$/NF (17.36 mF cm^{-2}) and NiFeO$_x$/NF (13.41 mF cm^{-2}). Furthermore, according to the ECSA value (Table S5, Supporting Information), RuPd-RuNiFeO$_x$/NF has the highest intrinsic activity.

As demonstrated in **Figure 4f**, the LSV curve of RuPd-RuNiFeOx/NF before and after 5,000 cycles for OER exhibits only a slight shift. Furthermore, the outcome of the chronoamperometric (i-t) evaluation (**Figure 4g**) demonstrates that the catalyst possesses the capacity to sustain consistent catalytic functionality for a duration of 80 h. This validates the long-term stability of RuPd-RuNiFeOx/NF in the context of OER. From Figure S14(Supporting Information), we can observe that the catalyst surface of RuPd-RuNiFeO$_x$/NF after 80 h OER test shows a high-density nanoparticle agglomerate structure compared with the pristine (Figure S5, Supporting Information). And the particle was stacked in a disordered manner in the form of spherical clusters, with a high-density exposure of active sites such as the alloy interfaces, and not obviously sintered, which provides a microstructure for OER processes. In addition, XPS and Raman

View Article Online
DOI: 10.1039/D5SC06809F

spectroscopic analyses of RuPd-RuNiFeO$_x$/NF after OER show that the surface oxidation occurred. The Ni2p spectra have no significant change, indicating that the surface Ni composition did not change. The positive peak shift of Fe2p and Pd3d indicates that the oxidation of Fe and Pd took place during the OER process (Figure S15a, b, Supporting Information). Note that, no new peaks appear for Ru3p, nor was there any significant shift, consistent with expectations. The special electron distribution can inhibit the excessive oxidation of Ru (Figure S15c, Supporting Information). The Pd3d orbitals have characteristic double peaks at 335.8 ($3d_{5/2}$) and 340.98 eV ($3d_{3/2}$), which correspond to the electronic structure of PdO_x (x<1) (Figure S15d, Supporting Information). In addition, Raman spectra further confirm the formation of metal oxides. Two new characteristic peaks appear at 474.1 and 544.3 cm^{-1} (Figure S16, Supporting Information), attributed to Ni-O vibrations, indicating the formation of NiOOH. [33] These oxides and hydroxides can continue to drive the reaction as additional active sites, reducing the adsorption energy of the intermediates and thus improving the OER performance of RuPd-RuNiFeO$_x$/NF.

The excellent HER and OER activities of RuPd-RuNiFeO$_x$/NF, characterized by ultralow overpotentials and favorable kinetics, are directly correlated with its distinctive interfacial electronic structure. XPS and EPR analyses confirm electron transfer from the NiFeO$_x$ support to the RuPd cluster via oxygen vacancies, resulting in an electron-rich state at the Ru active sites. This modulation of the electronic structure corresponds directly to the enhanced water dissociation capability in HER and the optimized reaction kinetics in OER, collectively contributing to the outstanding activity and stability of the catalyst for overall water splitting.

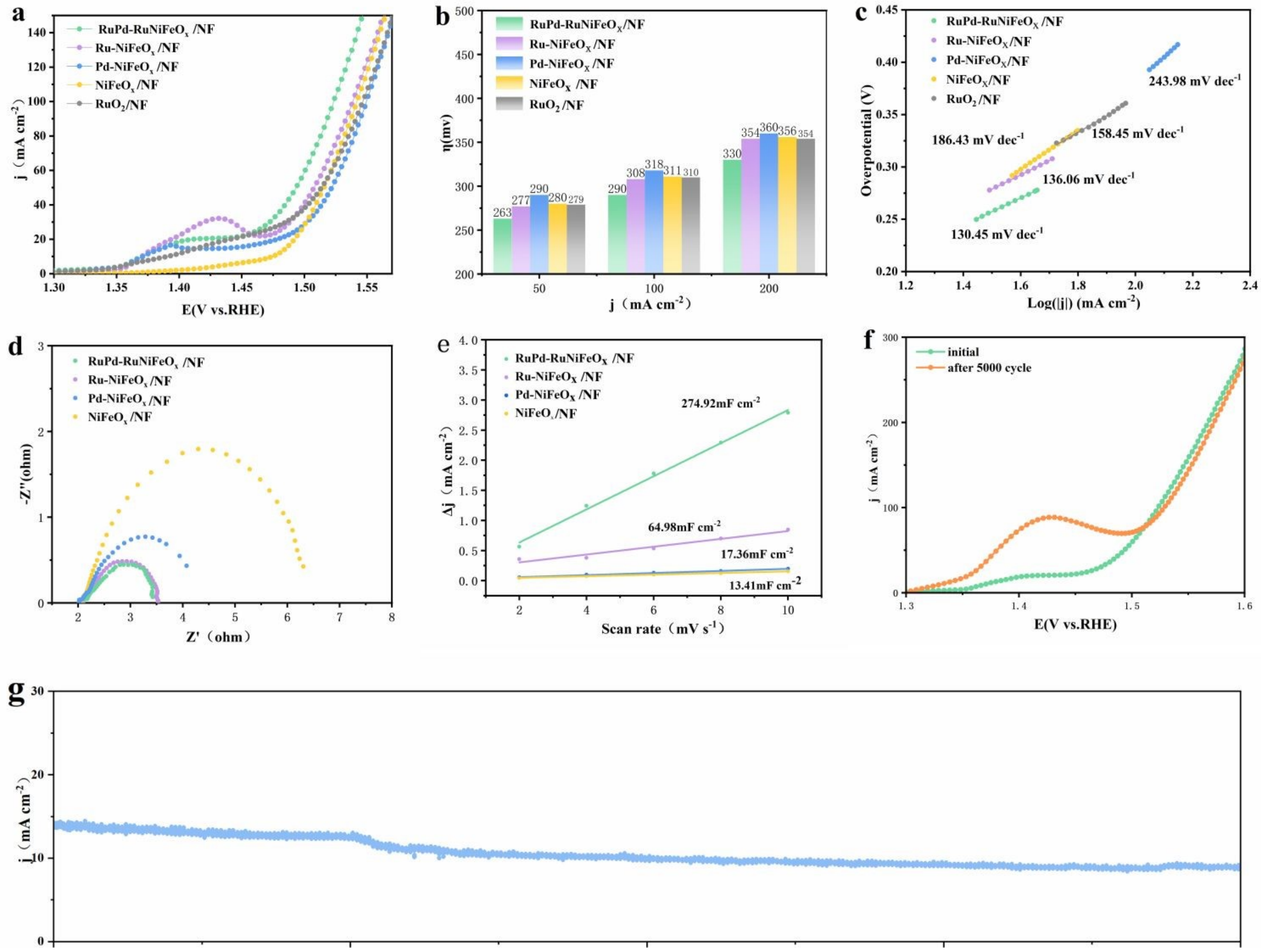

Fig. 4 a) OER polarization curves of various catalysts in alkaline freshwater. b) Corresponding overpotentials. c) Tafel slope. d) Nyquist plots. e) Plots of current density versus scan rate for various catalysts. f) LSV curves initially and after cycles of cyclic voltammetry. g) Chronoamperometric i-t tests of RuPd-RuNiFeO$_x$/NF.

2.3 Seawater and overall water splitting performance

The catalytic performance of the samples in alkaline seawater media was also investigated. As shown in **Figure 5a** and Figure S17 (Supporting Information), RuPd-RuNiFeO$_x$/NF exhibits excellent HER activity, requiring only 22 and 66 mV to achieve current densities of 10 and 50 mA/cm^2, respectively, superior to that of commercial Pt/C on NF in seawater (34 and 89 mV, respectively). Meanwhile, as shown in **Figure 5b** and Figure S19 (Supporting Information), it also exhibits excellent OER activity in seawater, with overpotentials as low as 283 and 312 mV at current densities of 50 and 100 mA/cm^2, respectively, superior to commercial RuO_2 catalysts on NF (326 and 399 mV, respectively) comparable to that of commercial RuO_2 catalysts on NF. In addition, RuPd-RuNiFeO$_x$/NF has a lower Tafel

View Article Online
DOI: 10.1039/D5SC06809F

slope (Figures S18 and S20, Supporting Information), also suggesting a rapid reaction kinetics in seawater.

Encouraged by the robust HER/OER properties, the RuPd-RuNiFeO$_x$/NF catalyst was further examined in symmetric overall water splitting (OWS) under alkaline media (**Figure 5c**). The RuPd-RuNiFeO$_x$/NF||RuPd-RuNiFeO$_x$/NF pair requires only 1.406 V to obtain a current density of 10 mAcm^{-2}， which exhibits excellent OWS performance in alkaline freshwater, which also outperforms the Pt/C||RuO^2 pair (1.51 V) as well as other catalysts reported recently (Table S6, Supporting Information). In addition, the RuPd-RuNiFeO$_x$/NF||RuPd-RuNiFeO$_x$/NF pair also exhibits excellent OWS activity (1.47 V@10 mAcm^{-2}) in seawater. And then, to achieve a larger current density of 100 mAcm^{-2}, under alkaline conditions, it requires only 1.66 and 1.75 V in alkaline freshwater and alkaline seawater, respectively. Although the presence of insoluble precipitates, bacteria and microorganisms in seawater passivates the active site, resulting in relatively low catalytic performance in alkaline seawater compared to that in alkaline, it still has the high catalytic activity in seawater.

As shown in **Figure 5d**,e, the LSV curves of RuPd-RuNiFeOx/NF before and after 5000 cycles only slightly shift. Meanwhile, the multi-step timed potential test (**Figure 5f**) shows that the catalyst has a stable gradient trend at different current densities, and the voltage remains almost unchanged after reaching 500 mAcm^{-2} at the same current density (100-500 mAcm^{-2}). In alkaline electrolytes, the RuPd-RuNiFeO$_x$/NF electrode can deliver a high OWS activity with a negligible attenuation rate for 100 h at 200 mAcm^{-2}. Undoubtedly, these prove that RuPd-NiFeO$_x$/NF has excellent durability. Besides, RuPd-RuNiFeOx/NF||RuPd-RuNiFeO$_x$/NF pair only has a weak performance degradation in seawater (Figures S21, Supporting Information), and the post-test SEM image (Figure S 22 and S 23, Supporting Information) reveals that the catalyst maintains its structural integrity without significant corrosion or aggregation after seawater electrolysis, further confirming its robustness.

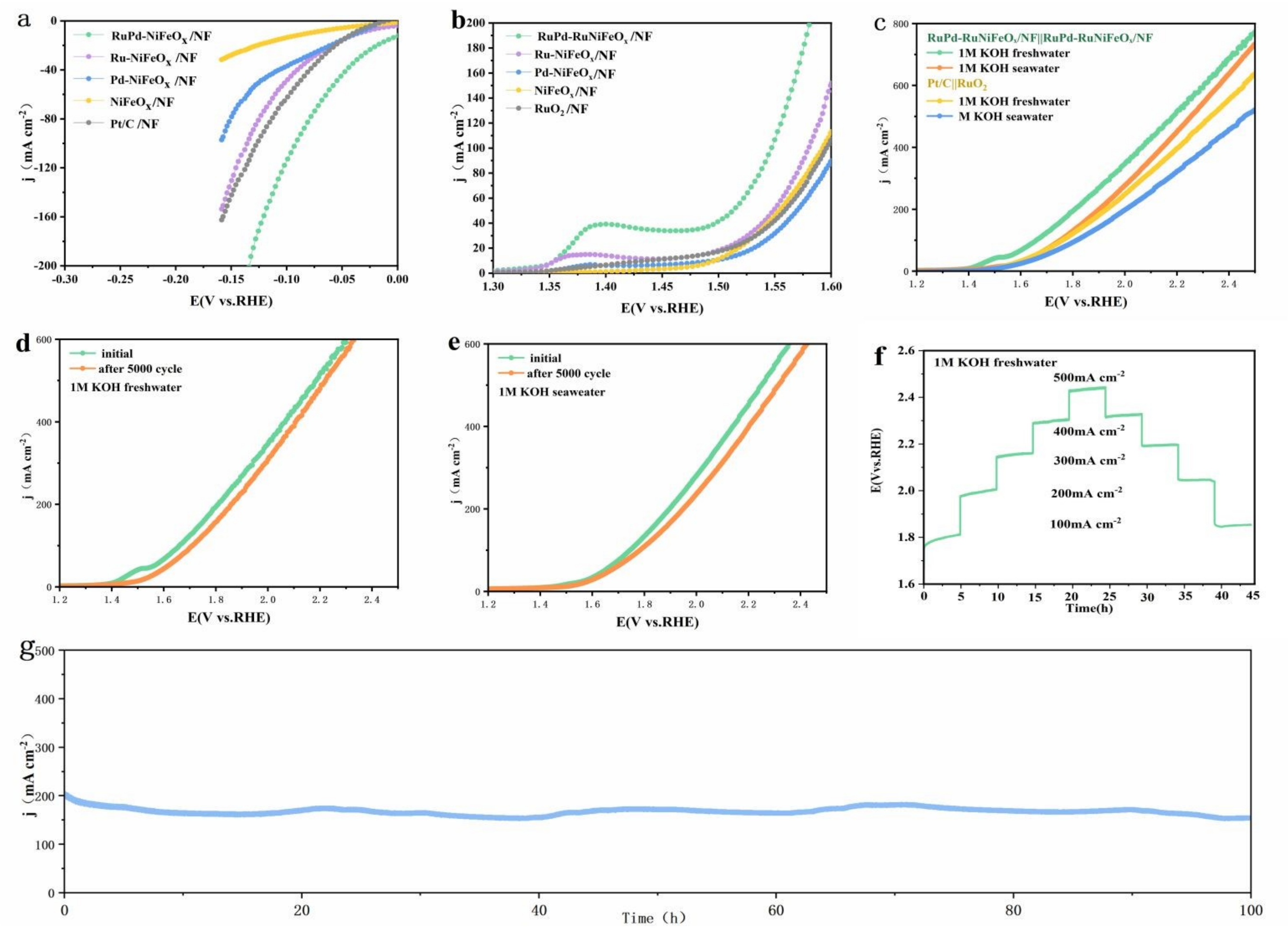

Fig. 5 a) HER and b) OER polarization curves for various catalysts in alkaline seawater. c) Polarization curves of RuPd-NiFeO$_x$/NF||RuPd-NiFeO$_x$/NF and Pt/C||RuO^2 on NF in alkaline freshwater and alkaline seawater. d) LSV curves in the initial state and after cycles e) in alkaline freshwater and f) Multicurrent chronopotentiometry response for RuPd-RuNiFeO$_x$/NF in alkaline freshwater. g) Chronoamperometric i-t tests of RuPd-RuNiFeO$_x$/NF||RuPd-RuNiFeO$_x$/NF at 200 mA cm^{-2} in alkaline electrolytes.

View Article Online
DOI: 10.1039/D5SC06809F

2.4 Theoretical calculation

To gain an in-depth understanding of the electronic structure and catalytic mechanism of the RuPd-RuNiFeO$_x$/NF catalyst at the atomic scale, density functional theory (DFT) calculations were performed. We constructed four representative theoretical models to systematically study the structure-activity relationship of catalysts: (1) A pure Pd(111) surface (Figure S24, Supporting Information), (2) a Ru-doped Pd(111) surface (Figure S25, Supporting Information), (3) a RuPd cluster supported on a NiFeO$_x$ surface with an oxygen vacancy (denoted as RuPd-NiFeO$_x$-Ov), used for HER simulations (Figure S26, S27, Supporting Information), to better simulate the significantly increased oxygen vacancy concentration in the catalyst due to the introduction of Ru/Pd (as evidenced in Fig. 2e, f), we introduced approximately 10% oxygen vacancies into the NiFeO$_x$ surface model, and constructed the RuPd-NiFeO$_x$-Ov model to reasonably reflect its modulatory effect on the interfacial electronic structure, (4) a RuPd cluster supported on a NiFeOOH surface (denoted as RuPd-NiFeOOH), used for OER simulations (Figure S28-S30, Supporting Information). The adsorption free energies (ΔG) of reaction intermediates were calculated using the standard hydrogen electrode (SHE) model.

Figure 6a and **b** shows the structural model of Ru-Pd(111), and the heterostructure model of PdRu-NiFeO$_x$-O$_V$, respectively. The charge redistribution at the RuPd/NiFeO$_x$ interface was investigated using differential charge density (DCD) analysis. As shown in **Figure 6c** (PdRu-NiFeO$_x$) and Figure S31 (RuPd-NiFeOOH), the isosurface of the differential charge density clearly reveals significant electron accumulation around the RuPd cluster and electron depletion in the adjacent NiFeO$_x$ support. This indicates a directional electron transfer from NiFeO$_x$ to RuPd. Therefore, the DFT calculations provide direct evidence for the electron enrichment effect at the RuPd sites in the catalyst, consistent with the XPS and EPR observations.

Given that water adsorption is a prerequisite for water splitting, we further calculated the H$_2$O adsorption energy (ΔE_{H_2O}) for Pd(111), Ru(001), Ru-Pd(111), and PdRu-NiFeO$_x$ systems. As shown in **Figure 6d**, the ΔE_{H_2O} of Ru-Pd(111) (−0.71 eV) is higher than that of Ru(001) (−0.54 eV) and Pd(111) (−0.48 eV), demonstrating that the presence of Pd can enhance water adsorption on Ru. In the PdRu-NiFeO$_x$ system, the ΔE_{H_2O} at the Ru site is higher than that at the Pd and Ni sites, confirming Ru as the genuine active center, in agreement with the XPS results. The higher ΔE_{H_2O} for PdRu-NiFeO$_x$ compared to Ru-Pd(111) suggests that the presence of NiFeO$_x$ renders the PdRu-NiFeO$_x$ surface more hydrophilic, beneficial for subsequent HER/OER catalytic steps. In the subsequent water dissociation process, PdRu-NiFeO$_x$-Ru exhibits the lowest H$_2$O dissociation barrier (0.31 eV), indicating its favorability for H$_2$O dissociation and H* intermediate formation (Figure S32, Supporting Information).

The hydrogen evolution reaction (HER) activity is closely related to the hydrogen adsorption free energy (ΔG_{H^*}). Then we calculated ΔG_{H^*}on different models to elucidate the role of electron enrichment. As shown in **Figure 6e**, the ΔG_{H^*} for the pure Pd(111) surface is -0.72 eV, indicating overly strong adsorption for HER. When Ru is doped into the Pd(111) surface, the ΔG_{H^*} becomes -0.54 eV, which is still not optimal. In contrast, the RuPd cluster supported on NiFeO$_x$-Vo exhibits a near-optimal ΔG_{H^*} of -0.10 eV (close to 0 eV). This nearly neutral ΔG_{H^*} in the heterostructure helps balance hydrogen adsorption/desorption behavior, thereby enhancing HER performance. This significant improvement is attributed to the electron enrichment effect at the RuPd site, which modulates the d-band center of Ru. As shown in **Figure 6f**, the d-band center of Ru in the RuPd-NiFeO$_x$ model shifts down by 0.12 eV compared to that in the Ru-doped Pd(111) model, leading to weaker H* adsorption and thus a more favorable ΔG_{H^*}.

For the oxygen evolution reaction (OER), we investigated the adsorption free energies of reaction intermediates (*OH, *O, and *OOH) on the RuPd-NiFeOOH model. The adsorption site for these intermediates on various systems is shown in Figures S28-S30 (Supporting Information). The OER free energy diagram is shown in **Figure 6g**. The overpotential is determined by the potential-limiting step (the step with the largest increase in free energy). The results show that the rate-determining step (RDS) for the Ni site is the transformation of *OH to *O (the *OH → *O step), while the RDS for both the Ru site and the Ru$_{sa}$ (single atom) site is also the *O → *OOH step. Notably, the RDS energy barriers for the Ru site at U = 0 V and U = 1.23 V (1.72 eV and 0.42 eV, respectively) are significantly lower than those for the Ni site (1.94 eV and 0.71 eV) and the Ru$_{sa}$ site (2.09 eV and 0.81 eV). It indicates that the Ru site exhibits the most favourable thermodynamic and kinetic properties, representing the true active center. To visually distinguish the OER pathway and energetic between the two distinct Ru configuration, the schematic illustration and corresponding free energy diagrams are provided in Figure S33 a and c to depict the reaction pathway and energy profile for the Ru site within the RuPd cluster, while Figure S33 b and d correspond to those for an isolated Ru single atom (Ru$_{sa}$). The direct comparison demonstrates that the Ru site in the cluster affords a more favourable reaction pathway with a lower energy barrier than the Ru$_{sa}$ site, confirming that the superior OER activity originates from the electron-enriched Ru within the RuPd cluster.

The stability of Ru-based catalysts is often limited by the over-oxidation and dissolution of Ru at high potentials. To understand the exceptional stability of our catalyst, we calculated the dissolution energies of Ru and Pd atoms in different environments. As shown in **Figure 6h**, the dissolution energies of Ru in the PdRu-NiFeO$_x$ (HER) and RuPd-NiFeOOH (OER) models are 15.72 eV and 13.14 eV, respectively, whereas it is 11.81 eV for Ru-Pd(111). This indicates that the atoms in our catalyst are thermodynamically less prone to dissolution. The enhanced stability is attributed to the electron enrichment at the Ru site, which reduces the tendency of Ru to lose electrons and form soluble high-valence species (e.g., RuO_4^{2-}). Therefore, the DFT calculation confirms that the designed electron-enriched structure not only enhances catalytic activity but also ensures long-term stability.

View Article Online
DOI: 10.1039/D5SC06809F

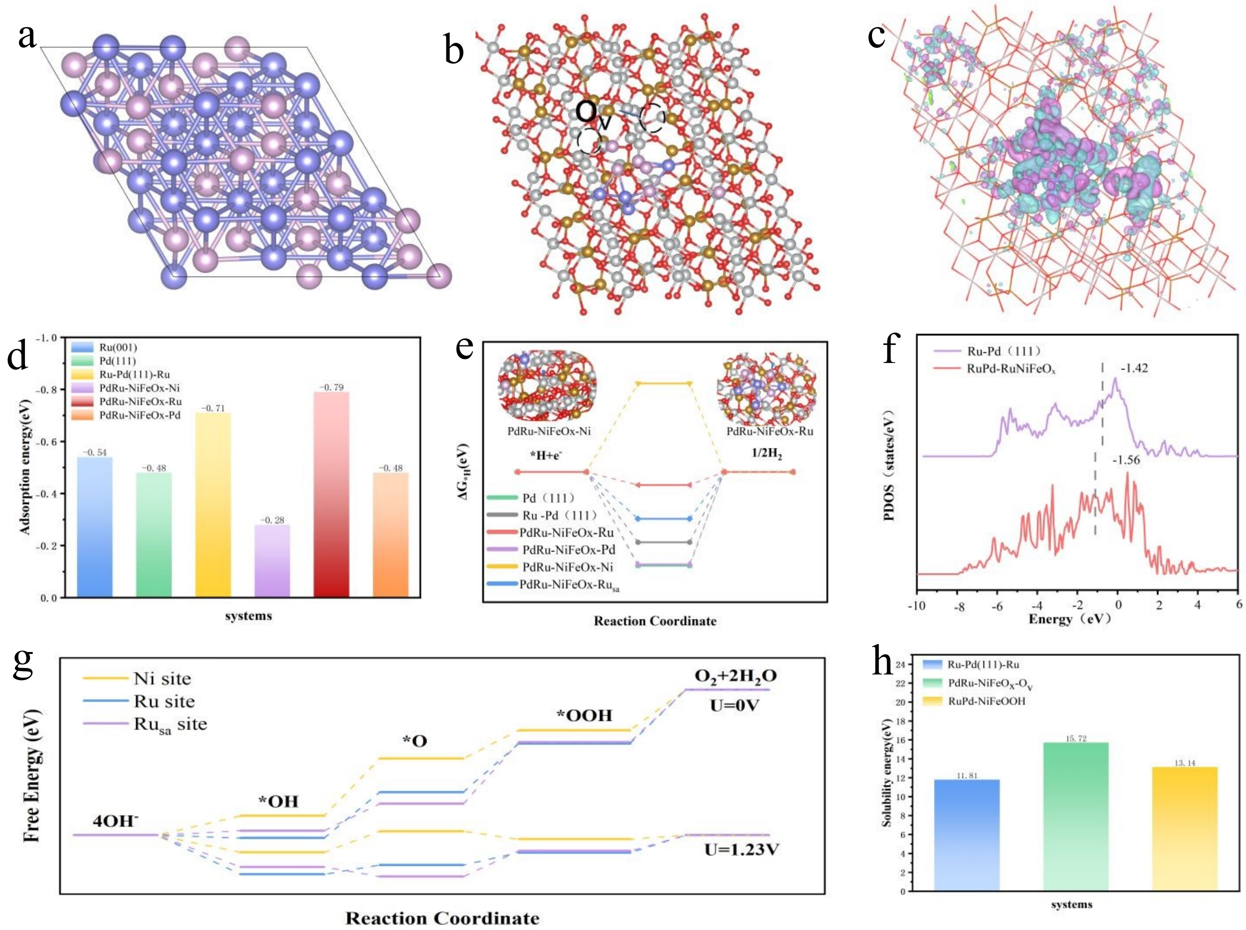

Fig. 6 Catalytic enhancement mechanism analyses. a) Structure model of Ru-Pd(111). b) Structure model of PdRu-NiFeOx-O_V. c) The DCD.d) ΔE_{H2O} on different sample surface. e) Energy barriers for HER at different sites. f) The partial density of states (PDOS) of Ru in Ru-Pd(111) and PdRu-$NiFeO_x$. g) OER free energy diagrams for RuPd-NiFeOOH. h) Solubility energy.

3. Conclusions

In summary, a high-performance RuPd-$RuNiFeO_x$/NF bifunctional catalyst was successfully fabricated via a straightforward non-homogeneous nucleation method. The catalyst demonstrates outstanding activity and durability for overall water splitting in both alkaline freshwater and seawater, requiring only 1.406 V to achieve 10 mA cm^{-2}. The exceptional performance is attributed to a synergistic mechanism elucidated through combined experimental and DFT calculation analysis: 1) Electron enrichment at Ru Sites: Interfacial charge transfer from the $NiFeO_x$ support to the RuPd cluster creates the electron enrichment on Ru as active center. 2) Optimized reaction energetics: This electronic configuration downshifts the d-band center of Ru, leading to optimized adsorption strengths for key intermediates, as evidenced by a near-neutral $\Delta G_{H^{**}}$and lowered OER energy barriers. 3) Enhanced structural stability: The electron-rich state of Ru substantially increases its dissolution energy, providing a robust thermodynamic barrier against over-oxidation and metal leaching, thereby ensuring long-term operational stability. This study not only presents a superior catalyst but also establishes "targeted electron enrichment" as a fundamental design principle, validated by multiscale evidences from atomistic simulations to macroscopic performance, paving the way for the rational development of advanced catalysts for green hydrogen economies.

Author Contributions

Yuqin Yin: investigation, scheme design, data collation, visualization, and writing. **Hongyu Zhao**: software, formal analysis. **Zhanghu Yu and Guanren Ge**: investigation, experimental testing, data collation, and verification. **Haoyu Zhou and Shiyuan Feng**: data curation, methodology and verification. **Kaiyang Sun:** experimental

View Article Online
DOI: 10.1039/D5SC06809F

testing. **Jie Du, Tong Chen and Zhihao Yang**: investigation, formal analysis, verification and data curation. **Jun Yu**: guidance, methodology, fund acquisition, and writing, review and editing. **Shichun Mu**: guidance, review, editing and fund acquisition.

Conflicts of interest

There are no conflicts of interest to declare.

Data Availability Statement

The data supporting this article have been included as part of the Supplementary Information.

Acknowledgements

This work was supported by the National Natural Science Foundation of China (Grant No. 22179104), the State Key Laboratory of Advanced Technology for Materials Synthesis and Processing (Wuhan University of Technology) (2025-ZD-2).

Notes and references

1 Z. W. Seh, J. Kibsgaard, C. F. Dickens, I. Chorkendorff, J. K. Nørskov and T. F. Jaramillo, *Science*, 2017, **355**, eaad4998.

2 X. Yang, L. Xu and Y. Li, *Coord. Chem. Rev.*, 2024, **516**, 215961.

3 J. Zhang, T. Wang, P. Liu, Z. Liao, S. Liu, X. Zhuang, M. Chen, E. Zschech and X. Feng, *Nat. Commun.*, 2017, **8**, 15437.

4 H. Ding, C. Su, J. Wu, H. Lv, Y. Tan, X. Tai, W. Wang, T. Zhou, Y. Lin, W. Chu, X. Wu, Y. Xie and C. Wu, *J. Am. Chem. Soc.*, DOI:10.1021/jacs.4c01379.

5 X. Huang, L. Gong, H. Xu, J. Qin, P. Ma, M. Yang, K. Wang, L. Ma, X. Mu and R. Li, *J. Colloid Interface Sci.*, 2020, **569**, 140–149.

6 X. Zhou, M. Mukoyoshi, K. Kusada, T. Yamamoto, T. Toriyama, Y. Murakami, S. Kawaguchi, Y. Kubota, O. Seo, O. Sakata, T. Ina and H. Kitagawa, *Chem. Sci.*, 2024, **15**, 7560–7567.

7 K. Li, Z. Tao, X. Ma, J. Wu, T. Wu, C. Guo, Y. Qi, J. Yu, J. Zheng and J. Xue, *Int. J. Hydrogen Energy*, 2025, **132**, 183–211.

8 T. Wang, Y. Yuan, W. Shi, G. Li, P. Rao, J. Li, Z. Kang and X. Tian, *Chem. Commun.*, 2025, **61**, 1719–1728.

9 Y. Xu, H. Lv, H. Lu, Q. Quan, W. Li, X. Cui, G. Liu and L. Jiang, *Nano Energy*, 2022, **98**, 107295.

10 S. Wang, A. Lu and C.-J. Zhong, *Nano Converg.*, 2021, **8**, 4.

11 Z.-J. Wu, J.-H. Li, J. Ying and C. Janiak, *Small*, **n/a**, 2504302.

12 Q.-N. Zhan, T.-Y. Shuai, H.-M. Xu, C.-J. Huang, Z.-J. Zhang and G.-R. Li, *Chin. J. Catal.*, 2023, **47**, 32–66.

13 H. Zhang, W. Liu, Z. Li, L. Qiao, K. Chi, X. Guo, D. Cao and D. Cheng, *Adv. Sci.*, 2024, **11**, 2401398.

14 X. Yang, Z. Wu, Z. Xing, C. Yang, W. Wang, R. Yan, C. Cheng, T. Ma, Z. Zeng, S. Li and C. Zhao, *Small*, 2023, **19**, 2208261.

15 R. Li, H. Zhao, L. Wang, Q. Zhou, X. Yang, L. Jiang, X. Luo, J. Yu, J. Wei and S. Mu, *Chem. Sci.*, 2025, **16**, 4383–4391.

16 J. Wang, X. Zhao, Y. Zhang, Y. Dong, Y. Yin, Z. Yu, G. Ge, J. Yu and S. Mu, *ACS Appl. Nano Mater.*, 2025, **8**, 631–638.

17 J. Zhao, Y. Guo, Z. Zhang, X. Zhang, Q. Ji, H. Zhang, Z. Song, D. Liu, J. Zeng, C. Chuang, E. Zhang, Y. Wang, G. Hu, M. A. Mushtaq, W. Raza, X. Cai and F. Ciucci, *Nat. Nanotechnol.*, 2025, **20**, 57–66.

18 P. Zhai, M. Xia, Y. Wu, G. Zhang, J. Gao, B. Zhang, S. Cao, Y. Zhang, Z. Li, Z. Fan, C. Wang, X. Zhang, J. T. Miller, L. Sun and J. Hou, *Nat. Commun.*, 2021, **12**, 4587.

19 Y. Yang, Q.-N. Yang, Y.-B. Yang, P.-F. Guo, W.-X. Feng, Y. Jia, K. Wang, W.-T. Wang, Z.-H. He and Z.-T. Liu, *ACS Catal.*, 2023, **13**, 2771–2779.

20 W. Yang, Y. Bai, L. Peng, M. Qu and K. Sun, *J Colloid Interface Sci.*, 2023, **648**, 701–708.

21 Y. Yang, Y. Xie, Z. Yu, S. Guo, M. Yuan, H. Yao, Z. Liang, Y. R. Lu, T.-S. Chan, C. Li, H. Dong and S. Ma, *Chem. Eng. J.*, 2021, **419**, 129512.

22 Z. Xie, C. Zhang, X. He, Y. Liang, D. Meng, J. Wang, P. Liang and Z. Zhang, *Front. Chem.*, 2019, **7**, 539.

23 A. Govind Rajan, J. M. P. Martirez and E. A. Carter, *Phys Chem Chem. Phys.*, 2024, **26**, 14721–14733.

24 S. Wu, D. Chen, S. Li, Y. Zeng, T. Wang, J. Zhang, J. Yu, S. Mu and H. Tang, *Adv. Sci.*, 2023, **10**, 2304179.

25 L. Chong, G. Gao, J. Wen, H. Li, H. Xu, Z. Green, J. D. Sugar, A. J. Kropf, W. Xu, X.-M. Lin, H. Xu, L.-W. Wang and D.-J. Liu, *Science*, 2023, **380**, 609–616.

26 P. Mondal, J. Satra, D. N. Srivastava, G. R. Bhadu and B. Adhikary, *ACS Catal.*, 2021, **11**, 3687–3703.

27 L. Jiang, L. Jiang, X. Luo, R. Li, Q. Zhou, W. Zeng, J. Yu, L. Chen and S. Mu, *eScience*, 2025, **5**, 100398.

28 Z. Li, G. Lin, L. Wang, H. Lee, J. Du, T. Tang, G. Ding, R. Ren, W. Li, X. Cao, S. Ding, W. Ye, W. Yang and L. Sun, *Nat. Catal.*, 2024, **7**, 944–952.

29 Y. Dong, Q. Sun, C. Zhan, J. Zhang, H. Yang, T. Cheng, Y. Xu, Z. Hu, C.-W. Pao, H. Geng and X. Huang, *Adv. Fun. Mater.*, 2023, **33**, 2210328.

30 Y. Cao, X. Lv, J. Yang, K. An, C. Liu, L. Qiao, Z. Yu, L. Li and H. Pan, *Dalton Trans.*, 2025, **54**, 9761–9769.

View Article Online
DOI: 10.1039/D5SC06809F

31 X. Mu, Y. Yuan, M. Yu, Y. Hu, W. Zeng, W. Peng, Y. Zhang, X. Liu, S. Liu and S. Mu, *Nano Energy*, 2024, **131**, 110216.

32 X. Zhang, Y. Xue, X. Yin, L. Shen, K. Zhu, X. Huang, D. Cao, J. Yao, G. Wang and Q. Yan, *J. Power Sources*, 2022, **540**, 231664.

33 P. Liu, B. Chen, C. Liang, W. Yao, Y. Cui, S. Hu, P. Zou, H. Zhang, H. J. Fan and C. Yang, *Adv. Mater.*, 2021, **33**, 2007377.

View Article Online
DOI: 10.1039/D5SC06809F

The data supporting this article have been included as part of the Supplementary Information.